

VIP Very Important Paper

www.batteries-supercaps.org

# Investigating the Influence of the Effective Ionic Transport on the Electrochemical Performance of Si/C-Arkyrodite Solid-State Composites

Yannik Rudel,<sup>[a]</sup> Moumita Rana,<sup>[a]</sup> Justine Ruhl,<sup>[a]</sup> Carolin Rosenbach,<sup>[a]</sup> Jannes Müller,<sup>[b]</sup> Peter Michalowski,<sup>[b]</sup> Arno Kwade,<sup>[b]</sup> and Wolfgang G. Zeier<sup>\*[a, c]</sup>

Solid-state batteries have the potential to outperform conventional lithium-ion batteries, as they offer higher energy densities, necessary for the increasing demand for portable energy storage. Silicon-graphite composites are considered to be one of the most promising alternatives to the lithium metal anode due to their low lithiation potential and resistance against dendrite formation. Since these composites show insufficient ionic conductivity, a fast-conducting solid electrolyte is needed to facilitate the charge carrier transport. Optimizing the volume fractions of the solid electrolyte is crucial to ensure sufficient charge carrier transport and achieve the optimal performance. In this work, the influence of the

charge carrier transport in a silicon on graphite (Si/C)/argyrodite solid electrolyte composite on the electrochemical performance is studied. By systematically varying the ratio of the Si/C to solid electrolyte, it was found that the effective ionic conductivity of the electrode composite improves exponentially with increasing content of the solid electrolyte, which in turn leads to an increase in the specific capacity of the composite across all C-rates. This study highlights the importance of understanding and customizing charge carrier transport properties in solid-state anode composites to achieve optimum electrochemical performance.

## Introduction

Solid-state batteries are seen as a possible successor to the conventional lithium-ion batteries, as they are estimated to offer higher energy densities, a wider operating temperature window and often are considered to be safer, as the flammable liquid electrolyte is replaced with a non-flammable solid electrolyte (SE).<sup>[1-3]</sup> One goal for solid-state-batteries is to use high capacity anode materials, with lithium metal being the most obvious candidate, as it has a high specific capacity. However, metallic lithium also poses some major drawbacks, as it is prone to dendrite formation as well as reactions with

electrolyte separators; here especially the sulfide-based SE form interphases.<sup>[4-7]</sup> Hence other materials are researched as possible high capacity anodes, such as silicon which is considered to be one of the most promising materials to be employed as an anode active material, it shows a high specific capacity ( $3590 \text{ mAh g}^{-1}$ ) and low lithiation potential (0.4 V vs. Li<sup>+</sup>/Li) compared to other anode materials.<sup>[8-10]</sup> However, the main drawback of employing silicon as an anode are the high volume changes during the lithiation/delithiation process (300%).<sup>[11-13]</sup> Since silicon itself is not sufficiently electronically or ionically conductive and needs conductive additives to perform well, the electrodes in Si-based are often composites of the active material, a SE and an electronically conductive additive such as carbon.<sup>[14-16]</sup>

Si-based composites with carbon as a conductive additive have been widely explored as potential candidates for use in lithium-ion batteries as well as solid-state-batteries.<sup>[17,18]</sup> In lithium-ion batteries it has been proven, that the volume changes caused by the lithiation and delithiation of silicon can be detrimental to the cells performance.<sup>[19]</sup> The relatively high amount of graphite used in the Si/C composite we employ in this work might provide a suitable buffer for these volume changes.<sup>[14]</sup> A silicon on graphite (Si/C) material which has a graphite content of 92%–93% exhibited good performance in a lithium-ion battery setup. The active material showed an initial specific discharge capacity of  $600 \text{ mAh g}^{-1}$  and was able to be cycled for 200 cycles with a capacity retention of  $\approx 50\%$  at a current density of  $1.23 \text{ mA cm}^{-2}$  for the first 100 cycles and  $2.06 \text{ mA cm}^{-2}$  for the remaining 50 cycles.<sup>[20]</sup> In order to investigate the influence of the charge carrier transport on the solid state battery performance, anode composites (AC) with

[a] Y. Rudel, Dr. M. Rana, J. Ruhl, C. Rosenbach, Prof. W. G. Zeier

Institute of Inorganic and Analytical Chemistry

University of Münster

Corrensstrasse 28/30, 48149 Münster (Germany)

E-mail: wzeier@uni-muenster.de

[b] J. Müller, Dr. P. Michalowski, Prof. A. Kwade

Institute for Particle Technology, and Battery LabFactory Braunschweig (BLB)

Technische Universität Braunschweig

Volkmaroder Str. 5, 38104 Braunschweig (Germany)

[c] Prof. W. G. Zeier

Institut für Energie- und Klimaforschung (IEK)

IEK-12: Helmholtz-Institut Münster Forschungszentrum Jülich

Corrensstrasse 40, 48149 Münster (Germany)

Supporting information for this article is available on the WWW under <https://doi.org/10.1002/batt.202300211>

© 2023 The Authors. Batteries & Supercaps published by Wiley-VCH GmbH. This is an open access article under the terms of the Creative Commons Attribution License, which permits use, distribution and reproduction in any medium, provided the original work is properly cited.

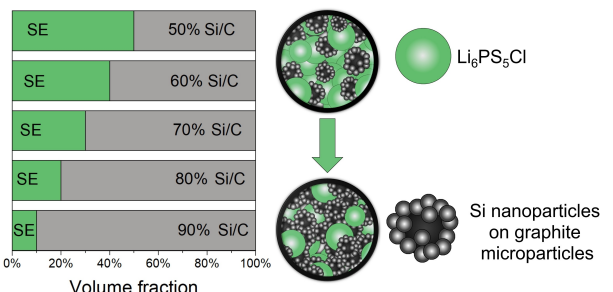


**Figure 1.** The variation of the volume fraction of the SE and the active material allows influencing the cell performance based on anode composition. The ratio of the SE to Si/C in the anode composite was varied between 50/50 vol.-% and 10/90 vol.-%.

varying volume fractions of SE and active material are prepared and studied for their electrochemical performance. With elucidating the cycling performance, using C-rate and stability test as well as analyzing the partial conductivities, it can be shown that the effective ionic conductivity in the anode composite improves with increasing solid electrolyte content, which in turn influences the accessible capacity and C-rate performance of the active.

## Results and Discussion

### Electrochemical performance

Composites with various volume fractions of the  $\text{Li}_6\text{PS}_5\text{Cl}$  and active material Si/C were prepared, as shown in Figure 1, to assess the influence of varying SE volume fractions in a Si/C-based anode composite on the cycling performance and rate capability. The volume ratios were calculated using the theoretical densities of the active material ( $\rho_{\text{Si/C}} = 2.26 \text{ g cm}^{-3}$ ) and the SE ( $\rho_{\text{SE}} = 1.89 \text{ g cm}^{-3}$ ). Figure S8 shows the scanning

electron micrograph images corresponding energy dispersive mappings of the composites as well as SEM images of the pristine and the processed active material. The uniform distribution of the elements throughout the scanning area supports the homogeneity of the components in the composite.

The electrochemical performance was first investigated by performing galvanostatic cycling tests for 50 cycles (Figure 2). The whole set of charge and discharge capacities as well as the Coulomb efficiencies for the different composites are shown in Figure S9; Exemplary charge and discharge profiles are given in Figure 2(b). It is apparent that lower contents of SE in the composite lead to a lower initial specific capacity. As the SE content decreases, the diffusion of lithium becomes kinetically slower, which could account for the observed behavior.<sup>[21]</sup> The anode composites containing 10 vol.-% SE and 50 vol.-% SE exhibit initial discharge capacities of  $132 \text{ mAh g}^{-1}$  and  $345 \text{ mAh g}^{-1}$ , respectively (Figure 2a). The capacity retention of the composites decreases from 82% to 69%, then to 58%, and eventually reaches 56% as the solid electrolyte fraction increases from 10 vol.-% SE to 40 vol.-% SE over the course of 50 cycles. However, the composite containing 50 vol.-% SE shows a higher capacity retention of 67%. Overall, a higher content of SE in the composite results in faster capacity fading in contrast to the ones with lower SE content. Figure 2(b) shows the comparison of the charge–discharge profiles of the anode composites with 50 vol.-% SE and 10 vol.-% SE for the 1<sup>st</sup>, 25<sup>th</sup> and 50<sup>th</sup> cycle. During charging, the overpotential of the half-cells for all anode composites containing more than 20 vol.-% SE (Figure S7) visibly increase. This indicates possible interphase formation potentially inhibiting charge carrier transport. Therefore, the decline in specific capacity may be attributed to a decomposition reaction of the SE and the carbon in the anode composite.<sup>[22,23]</sup>

The C-rate performance test shown in Figure 3(a) highlights that additional to the higher accessible capacity seen at 0.1 C at higher SE volume fraction, this trend is also observed at higher

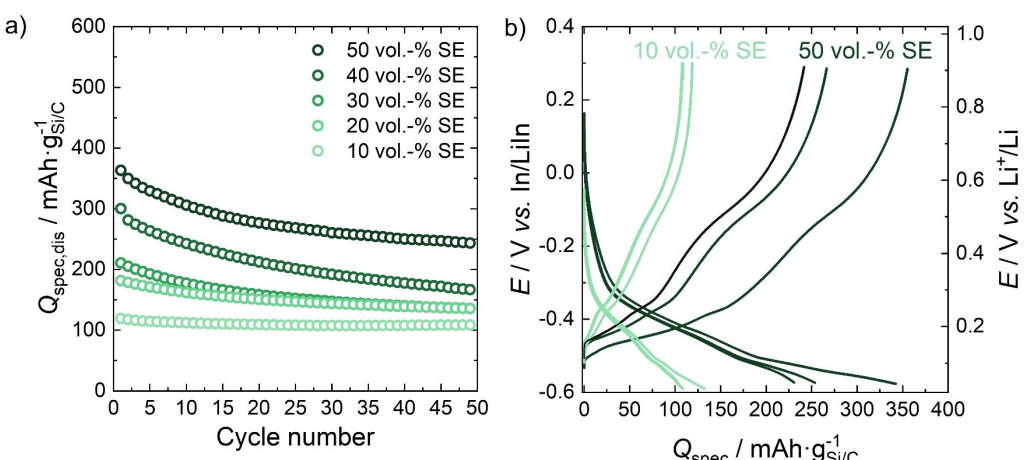


**Figure 2.** a) Stability test results of half cells with the various anode composites given by the specific discharge capacity in relation to the active material mass versus the cycle number. b) Charge/Discharge curves for the 1<sup>st</sup>, 25<sup>th</sup> and 50<sup>th</sup> cycle of the half cell with the anode composites containing 10 vol.-% SE and 50 vol.-% SE, respectively.

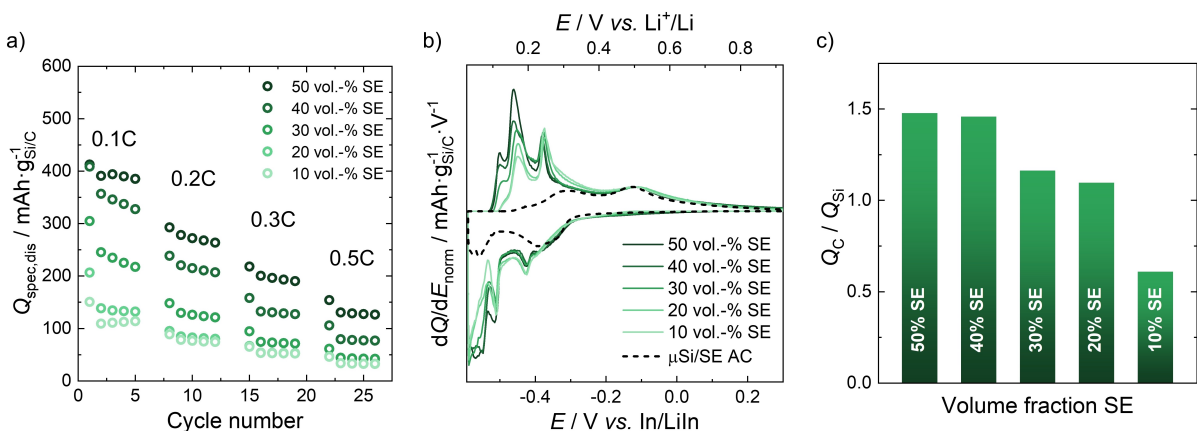


**Figure 3.** a) Rate capability test results of the different anode composites given by the specific discharge capacity in relation to the active material mass versus the cycle number. b) The derivative of the specific capacity in the second rate cycle (0.1 C) normalized to the highest silicon peak at  $-0.12$  V vs. In/LiIn as a function of the potential for each anode composite with Si/C and one composite with silicon micro-particles as a reference is shown. c) The ratio of accessed graphite ( $Q_c/Q_{Si}$ ) to accessed silicon charge for each composite, estimated by the areas in the  $dQ/dE$  graph.

C-rates. However, the capacity retention here shows a similar trend to the stability test, as the composites with higher volume fractions of SE generally show more pronounced capacity fading. To shed light on the positive correlation between an enhanced specific capacity of the Si/C-based composite with increasing SE content, the redox features of these mixtures were studied using the  $dQ/dE$  plots at the lowest C-rate (0.1 C,  $0.42$  mA cm $^{-2}$ ) (Figure S10a). From the aforementioned figure it is apparent that the total area under the respective curves, and with that the total amount of transferred charge increases with higher SE content. The reduction peaks at  $0.16$  V and  $0.25$  V vs. Li $^{+}$ /Li are related to the lithiation of graphite.<sup>[16,24]</sup> Additionally, a Si peak is forming a shoulder at the carbon peak at  $0.32$  V.<sup>[16,24]</sup> The peak at  $0.50$  V is a combination of Si and C.<sup>[16,24]</sup> The oxidation peaks are more convoluted compared to the reduction peaks, with Si showing two broad peaks at  $0.06$  V and  $0.24$  V.<sup>[16,24]</sup> However both Si peaks are overlayed with C peaks at  $0.03$  V,  $0.12$  V and  $0.2$  V.<sup>[16,24]</sup> Figure 3(b) shows the normalized voltage derivative of the specific capacity (2<sup>nd</sup> cycle at 0.1 C) against the voltage. A reference measurement using a cell with an anode composite containing silicon microparticles, carbon black and Li<sub>6</sub>PS<sub>5</sub>Cl in the weight ratio 35:5:60 is displayed in the plot as a dashed line. The  $dQ/dE$  plots are normalized with respect to the highest silicon peak that is least overlapping with a carbon peak at  $0.50$  V to quantitatively assess information about how the active material is utilized in the anode composite. The whole area inside the dashed line (Figure 3b) corresponds to contribution of silicon towards the total specific capacity, while the residual areas correspond to the contributed capacity by graphite.

From the normalized  $dQ/dE$  plots, the contribution of Si and C towards the total specific capacity can be estimated by integrating the total area under the plot and subtracting the contribution from the Si reference measurement. The estimated ratio corresponding to the contribution of the graphite-to-silicon area is shown in Figure 3(c). With increasing SE more graphite capacity is accessed. However, for the composite with

10 vol.-% SE, more silicon than graphite is accessed (Figure S10b). The Li $^{+}$  diffusion coefficient of non-lithiated graphite is higher compared to non-lithiated silicon, further supporting the relatively higher utilization of graphite in the composite.<sup>[25,26]</sup> The EDS images from the composites indicate that the Si particles are distributed through the anode composite during mixing, not staying completely attached to the graphite, which inherently leads to the electronic disconnection of the silicon in the anode material (Figure S8). This observation also explains why, relatively to silicon less graphite is utilized for composites with lower SE content, as more silicon is in contact with graphite and thus electronically better connected compared to the composites with higher SE content.

### Effective conductivities

To evaluate the influence of charge transport in the composite anodes on the specific capacity, the effective ionic and electronic conductivity are determined. The direct current resistance of the anode composite is measured using either an electron-blocking or an ion-blocking configurations for Li $^{+}$  or electron transport, respectively (Figure 4a). The details of the effective electronic and ionic conductivity measurements are given in Figures S11–S15. Figure 4(a) shows the respective effective ionic and electronic conductivities for the composites in relation to the volume fraction of the solid electrolyte. It is apparent that the effective ionic conductivity increases exponentially with higher fractions of SE in the anode composite going from the  $\mu$ S cm $^{-1}$  regime for the anode composites up to  $2.16$  mS cm $^{-1}$  for pristine Li<sub>6</sub>PS<sub>5</sub>Cl. A similar behaviour has been reported for other sulfur-based SEs as well, where higher contents of SE led to higher effective ionic conductivities. However, the exponential behaviour for the effective ionic conductivity in different systems is not always seen in other literature. Dewald et al. reported an exponential behaviour, while Ohno et al. and Minnmann et al. observed a different

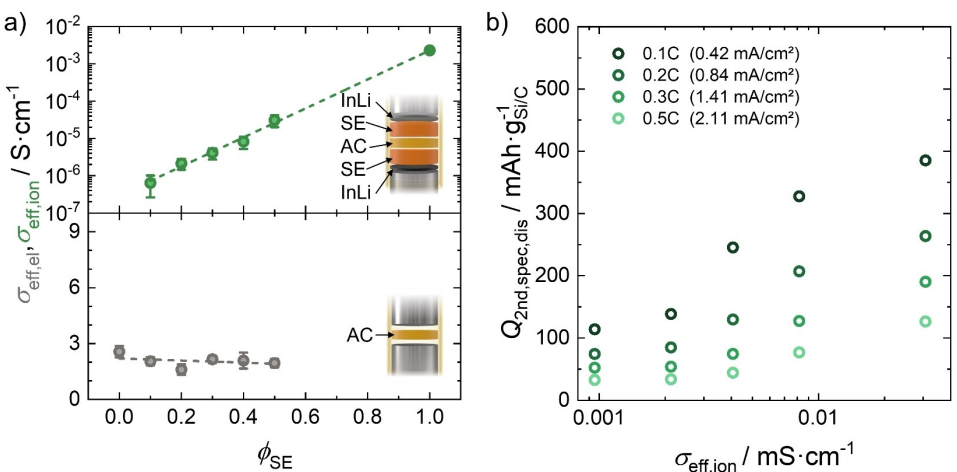


**Figure 4.** a) Effective ionic (logarithmic scale) and electronic (linear scale) conductivity of the anode composite in relation to the nominal volume fraction of the SE. The respective cell setups for the direct current polarization measurements are shown as insets. b) The discharge capacity of the second cycle for each rate is given in respect to the effective ionic conductivity.

trend.<sup>[21,27,28]</sup> These differences are most likely due to different pore size, shape and their relative distribution depending on the system.<sup>[29,30]</sup> In contrast to the changing effective ionic transport, the effective electronic conductivity remains constant at around  $2 \text{ Scm}^{-1}$ . This is five orders of magnitude higher than the effective ionic conductivity in all composites and as the graphite content in the anode composite is high enough for the changing composition to not have any effect on the effective electronic transport. Since the effective electronic conductivity is much higher than the effective ionic conductivity and does not significantly vary with the change in volume fraction of the SE in the composite, it is reasonable to assume that only the effective ionic conductivity accounts for the observed changes in specific capacity at different C-rates. Figure 4(b) shows the dependence of specific discharge capacity of the second cycle at each C-rate on the effective ionic conductivity of the anode composites. Clearly, the effective ionic conductivity have a significant influence on the accessible capacity for all C-rates, as the specific capacity shows an exponential dependency on  $\sigma_{\text{eff},\text{ion}}$  as higher effective ionic conductivities increase the specific discharge capacity. As stated before, optimizing the anode composite composition is important to access as much active material as possible. While the specific capacity increases almost linearly with the higher SE volume fractions, the effective ionic conductivity does not (Figure S16). This contrasts with other results reported in literature, where the specific capacity reaches a peak and decreases again, despite the effective ionic conductivity increasing.<sup>[21,31]</sup> In these reports however, the effective electronic conductivity is also changing, leading to an optimal ratio between effective electronic and ionic transport in the composite. Contrary to this, in the results shown here, only the effective ionic conductivity is changed and the effective electronic conductivity stays at a constant high value, meaning that solely the effective ionic conductivity affects the specific capacity and thus explaining why the specific capacity only increases.<sup>[21,27]</sup>

Overall, it seems that with more solid electrolyte, a lower tortuosity factor for  $\text{Li}^+$  transport in the anode (see Supporting Information) and faster transport can be achieved that in turn act beneficial on the attainable capacities.

## Conclusions

This work demonstrates the influence of the effective ionic conductivity on the electrochemical performance of a Si/C-based anode composites by systematically varying the ratio of the solid electrolyte  $\text{Li}_6\text{PS}_5\text{Cl}$  to the active material and exploring the electrochemical behaviour through rate capability and long-term cyclability tests. A nonlinear dependence between the specific capacity of anode composite and the ionic and electronic effective ionic conductivity is revealed. The constant effective electronic transport in all prepared composites enables the potential for a better comprehension of the significance of effective ionic conductivity in the anode composite. Consistently across all tested current densities, a lower ionic conductivity negatively impacts the cell performance. Although, the specific capacity values at low current density start to level out after certain effective ionic conductivity of  $8 \mu\text{S}\cdot\text{cm}^{-1}$ , this work shows that for high power applications it is important to design electrode composites with high effective ionic conductivity. Furthermore, the importance of understanding and tailoring transport properties in all solid-state anode composites is underlined in this work.

## Experimental Section

### Synthesis and characterization of the SE

All samples were handled under argon atmosphere [ $p(\text{O}_2) \leq 1 \text{ ppm}$   $p(\text{H}_2\text{O}) \leq 1 \text{ ppm}$ ]. The SE  $\text{Li}_6\text{PS}_5\text{Cl}$  was synthesized in 1.5 g batches in a solid-state synthesis. The precursors  $\text{Li}_2\text{S}$  (Alfa-Aesar, 99.9%),  $\text{LiCl}$  (Alfa-Aesar, 99%),  $\text{P}_2\text{S}_5$  (Sigma-Aldrich 99%) were stoichiometrically

cally mixed for 15 minutes in an agate mortar. The powder was then pressed into pellets, which were transferred into carbon-coated quartz glass ampules that had been dried at 800 °C in dynamic vacuum for 2 h. The ampules were sealed under vacuum and annealed in a tube furnace at 550 °C for 14 days with a heating rate of 100 °C/h followed by natural cooling. The pellets were hand-ground for further use and analysis. The purity of the SE was verified by X-Ray powder diffraction (Stoe STADI P,  $2\theta = 10^\circ$ – $80^\circ$ , Cu  $K_\alpha$   $\lambda = 1.54 \text{ \AA}$ ) (Figure S5a) and the ionic conductivity was determined by impedance spectroscopy using a BioLogic VMP-300 Potentiostat (Figure S5b) in a symmetrical press cell setup using 200 mg of SE with stainless-steel stamps as current collectors. For the measurement, the cells were fixed to an Al-frame and pressure was applied by a screw with a torque of 10 Nm (70 MPa).<sup>[32]</sup>

### Preparation of the anode composite

In-depth information on the Si/C active material (10 wt.% Si, 90 wt.% C) can be found in the references.<sup>[20]</sup> For the preparation of the anode composites with different volume ratios (Table S1) of Si/C and Li<sub>6</sub>PS<sub>5</sub>Cl, the active material and the SE were mixed in a shaker mill (Fritsch, PULVERISETTE 23). The mixing was done with a shaking frequency of 45 Hz for 10 minutes in a 15 mL ZrO<sub>2</sub> cup using 15 ZrO<sub>2</sub> balls with a diameter of 3 mm. For reference, a Si based composite was prepared in the same way by using a mixture of Si microparticles (<5 μm, Goodfellow) (35 wt.%) carbon black (ANR Technologies, Ketjenblack ECP600JD) (5 wt.%) and Li<sub>6</sub>PS<sub>5</sub>Cl (60 wt.%).

### Cell assembly

All cells were assembled in a custom-made brass casing around a PEEK inset with an inner diameter of 10 mm. Stainless-steel stamps were used as current collectors. For the electrochemical measurement, the cells were put into an Al-frame and a pressure is applied by a screw with a torque of 10 Nm (70 MPa).<sup>[32]</sup> The half-cells were assembled first by hand pressing 60 mg of Li<sub>6</sub>PS<sub>5</sub>Cl in the PEEK casing for five minutes. After that, the anode composite with 5.5 mg of active material was added on one side of the Li<sub>6</sub>PS<sub>5</sub>Cl separator. At this point it is necessary to note, that one must decide whether to maintain a constant total anode composite mass or keep the active material mass the same. The former may result in the use of thicker electrodes, which artificially yields unfavorable cell performance, while the latter may lead to lower loading and artificial improvement of the cell characteristics.

In this work, different total masses of anode composite were used while keeping the active material mass constant to allow for a fair comparison of the composites, as an increased volume fraction of solid electrolyte would inherently lead to shorter pathways in electrodes with constant composite mass. The cell was then pressed with a uniaxial press applying 374 MPa for three minutes. After that an indium (chemPUR, 100 μm thickness, 99.99%) disc (9 mm, 50 mg) followed by a freshly pressed lithium (abcr, 99.8%) disc (4 mm, 1.5 mg) was added to the other side of the separator.

For the ionic direct current polarization measurements 80 mg of Li<sub>6</sub>PS<sub>5</sub>Cl was first put into the cell, followed by 10 mg of the anode composite and another 80 mg of Li<sub>6</sub>PS<sub>5</sub>Cl. After adding each layer, the powder was hand-pressed for five minutes. The cell was then uniaxially pressed at 374 MPa for three minutes. Indium and lithium foils were then added to both sides of the cell, in a similar way as for the half-cell (Figure 4a, top). The electronic direct current polarization cell was assembled by putting 30 mg of the anode composite in the press cell (Figure 4a, bottom), and pressing at 374 MPa for three minutes. For the measurement, the cells were

fixed to an Al-frame and a screw with a torque of 10 Nm applied the pressure (70 MPa).<sup>[32]</sup>

### Electrochemical measurements

Before the cells were cycled, a resting period of 12 h was set to equilibrate the pressure in the cell and ensure the full microstructural relaxation.<sup>[33]</sup> The half-cells for the rate capability test were cycled with a BioLogic VMP-300 between 0.03 V and 0.9 V vs. Li<sup>+</sup>/Li. The cells were cycled for five cycles each at 0.1 C (0.42 mA cm<sup>-2</sup>), 0.2 C (0.84 mA cm<sup>-2</sup>), 0.3 C (1.41 mA cm<sup>-2</sup>) and 0.5 C (2.11 mA cm<sup>-2</sup>). After each C-rate, the cells were cycled at 0.1 C for two cycles to make sure that the anode composite is fully delithiated. The cells for the stability test were pre-cycled at 0.05 C (0.82 mA cm<sup>-2</sup>) for five cycles, in order to reduce contact loss induced by too fast volume changes of the Si during lithiation/delithiation followed by 50 cycles at 0.1 C (1.28 mA cm<sup>-2</sup>). Exemplary voltage profiles are given in the Supporting Information in Figure S6 for the rate capability test, Figure S7 for the long-term cycling.

The direct current polarization measurements for obtaining the effective ionic and electronic conductivity were performed using a Metrohm AutoLab Potentiostat. For all cells with a SE content in the composite between 50 vol.-% and 40 vol.-% the used voltages were 2.5 mV, 5 mV, 7.5 mV, 10 mV, 15 mV, 20 mV and 25 mV. For 30 vol.-% SE and less, the applied voltages were between 20 mV and 40 mV; higher voltages were needed to achieve measurable currents, the voltage was increased in five millivolt steps. Each voltage was held for five hours, as this was enough time for the current to equilibrate. Between the separate voltage steps a resting time of one hour was set to equilibrate the cell. The voltages applied for determining the effective electronic conductivity were –5 mV and 5 mV followed by 5 mV steps up to –25 mV while switching the direction of the applied voltage after each step. The voltages were held for three hours each, with a resting time of 15 minutes after each step. The anode composite resistance  $R_{\text{eff},\text{ion}}$  from which the effective ionic conductivity  $\sigma_{\text{eff},\text{ion}}$  is calculated, was obtained by subtracting the SE resistance contribution from the total measured resistance.

### Microscopic characterization

A Carl Zeiss scanning electron microscope (SEM) with an Auriga CrossBeam working station with a field emission gun (Schottky-type) was used to analyze pellets of the different anode composites before cycling as well as from the pristine and processed active material powder under an acceleration voltage of 3 kV. An InLense secondary electron detector was used for imaging. To investigate the composition of the composites and energy-dispersive X-ray spectroscopy (EDS) measurement was performed with an X-Max 80 mm<sup>2</sup> detector at an acceleration voltage of 15 kV.

### Supporting Information

In the Supporting Information a Pawley fit of the X-Ray diffraction pattern and an impedance spectrum of the solid electrolyte can be found. Furthermore, additional cycle data from the stability and rate performance tests are provided together with the volume and weight ratios used for the anode composite preparation. Scanning electron micrographs as well as EDS images are provided. The DC-polarization data is also provided. Additionally, a deeper discussion on tortuosity factors

can be found in the Supporting Information. Additional references cited in the supporting information.<sup>[34–51]</sup>

## Acknowledgements

The authors acknowledge financial support within the SiLK-ompAs funded by Bundesministerium für Bildung und Forschung (BMBF; projects 03XP0486B and 03XP0486 C). Moumita Rana acknowledges funding from the Alexander von Humboldt foundation. Open Access funding enabled and organized by Projekt DEAL.

## Conflict of Interests

The authors declare no conflict of interest.

## Data Availability Statement

The data that support the findings of this study are available from the corresponding author upon reasonable request.

**Keywords:** charge carrier transport · silicon-carbon composite anode · solid state batteries · sulfide solid electrolyte

- [1] L. Liu, J. Xu, S. Wang, F. Wu, H. Li, L. Chen, *eTransportation* **2019**, *1*, 100010.
- [2] A. M. Bates, Y. Preger, L. Torres-Castro, K. L. Harrison, S. J. Harris, J. Hewson, *Joule* **2022**, *6*, 742–755.
- [3] J. G. Kim, B. Son, S. Mukherjee, N. Schuppert, A. Bates, O. Kwon, M. J. Choi, H. Y. Chung, S. Park, *J. Power Sources* **2015**, *282*, 299–322.
- [4] Y. Zhu, X. He, Y. Mo, *ACS Appl. Mater. Interfaces* **2015**, *7*, 23685–23693.
- [5] K. B. Hatzell, X. C. Chen, C. L. Cobb, N. P. Dasgupta, M. B. Dixit, L. E. Marbella, M. T. McDowell, P. P. Mukherjee, A. Verma, V. Viswanathan, A. S. Westover, W. G. Zeier, *ACS Energy Lett.* **2020**, *5*, 922–934.
- [6] Y. Zhu, X. He, Y. Mo, *J. Mater. Chem. A* **2016**, *4*, 3253–3266.
- [7] Z. Wu, X. Li, C. Zheng, Z. Fan, W. Zhang, H. Huang, Y. Gan, Y. Xia, X. He, X. Tao, J. Zhang, *Electrochem. Energy Rev.* **2023**, *6*, DOI: 10.1007/s41918-022-00176-0.
- [8] R. A. Sharama, R. N. Seefurth, *Fluid Phase Equilib.* **1976**, *123*, 1763–1768.
- [9] M. Ashuri, Q. He, L. L. Shaw, *Nanoscale* **2016**, *8*, 74–103.
- [10] I. Na, H. Kim, S. Kunze, C. Nam, S. Jo, H. Choi, S. Oh, E. Choi, Y. B. Song, Y. S. Jung, Y. S. Lee, J. Lim, *ACS Energy Lett.* **2023**, 1936–1943.
- [11] Y. Yang, W. Yuan, W. Kang, Y. Ye, Q. Pan, X. Zhang, Y. Ke, C. Wang, Z. Qiu, Y. Tang, *Sustain. Energy Fuels* **2020**, *4*, 1577–1594.
- [12] M. T. McDowell, S. W. Lee, W. D. Nix, Y. Cui, *Adv. Mater.* **2013**, *25*, 4966–4985.
- [13] P. Vadhra, A. M. Boyce, A. Hales, M.-C. Pang, A. N. Patel, P. R. Shearing, G. Offer, A. J. E. Rettie, *J. Electrochem. Soc.* **2022**, *169*, 100525.
- [14] D. Cao, T. Ji, A. Singh, S. Bak, Y. Du, X. Xiao, H. Xu, J. Zhu, H. Zhu, *Adv. Energy Mater.* **2023**, 2203969, 1–13.
- [15] A. Franco Gonzalez, N. H. Yang, R. S. Liu, *J. Phys. Chem. C* **2017**, *121*, 27775–27787.
- [16] S. B. Son, L. Cao, T. Yoon, A. Cresce, S. E. Hafner, J. Liu, M. Groner, K. Xu, C. Ban, *Adv. Sci.* **2019**, *6*, 1–8.
- [17] H. Huo, J. Janek, *ACS Energy Lett.* **2022**, *7*, 4005–4016.
- [18] F. Dou, L. Shi, G. Chen, D. Zhang, *Electrochem. Energy Rev.* **2019**, *2*, 149–198.
- [19] S. J. Lee, J. K. Lee, S. H. Chung, H. Y. Lee, S. M. Lee, H. K. Baik, *J. Power Sources* **2001**, *97–98*, 191–193.
- [20] J. Müller, M. Abdollahifar, A. Vinograd, M. Nöske, C. Nowak, S. J. Chang, T. Placke, W. Haselrieder, M. Winter, A. Kwade, N. L. Wu, *Chem. Eng. J.* **2021**, *407*, 126603.
- [21] G. F. Dewald, S. Ohno, J. G. C. Hering, J. Janek, W. G. Zeier, *Batteries & Supercaps* **2021**, *4*, 183–194.
- [22] L. Peng, C. Yu, Z. Zhang, H. Ren, J. Zhang, Z. He, M. Yu, L. Zhang, S. Cheng, J. Xie, *Chem. Eng. J.* **2022**, *430*, 132896.
- [23] W. Zhang, T. Leichtweiß, S. P. Culver, R. Koerver, D. Das, D. A. Weber, W. G. Zeier, J. Janek, *ACS Appl. Mater. Interfaces* **2017**, *9*, 35888–35896.
- [24] L. J. Krause, T. Brandt, V. L. Chevrier, L. D. Jensen, *J. Electrochem. Soc.* **2017**, *164*, A2277–A2282.
- [25] N. Ding, J. Xu, Y. X. Yao, G. Wegner, X. Fang, C. H. Chen, I. Lieberwirth, *Solid State Ionics* **2009**, *180*, 222–225.
- [26] Z. Y. Tang, J. J. Xue, C. Y. Liu, X. G. Zhuang, *Acta Phys. Chim. Sin.* **2001**, *17*, 388.
- [27] P. Minnmann, L. Quillman, S. Burkhardt, F. H. Richter, J. Janek, *J. Electrochem. Soc.* **2021**, *168*, 040537.
- [28] S. Ohno, C. Rosenbach, G. F. Dewald, J. Janek, W. G. Zeier, *Adv. Funct. Mater.* **2021**, *31*, 1–14.
- [29] T. Bernges, T. Böger, O. Maus, P. S. Till, M. T. Agne, W. G. Zeier, *ACS Mater. Lett.* **2022**, *4*, 2491–2498.
- [30] D. A. G. Bruggeman, *Ann. Phys.* **1935**.
- [31] T. A. Hendriks, M. A. Lange, E. M. Kiens, C. Baeumer, W. G. Zeier, *Batteries & Supercaps* **2023**, DOI:10.1002/batt.202200544.
- [32] W. Zhang, D. A. Weber, H. Weigand, T. Arlt, I. Manke, D. Schröder, R. Koerver, T. Leichtweiss, P. Hartmann, W. G. Zeier, J. Janek, *ACS Appl. Mater. Interfaces* **2017**, *9*, 17835–17845.
- [33] R. Koerver, W. Zhang, L. De Biasi, S. Schweidler, A. O. Kondrakov, S. Kolling, T. Brezesinski, P. Hartmann, W. G. Zeier, J. Janek, *Energy Environ. Sci.* **2018**, *11*, 2142–2158.
- [34] J. Landesfeind, J. Hattendorff, A. Ehrl, W. A. Wall, H. A. Gasteiger, *J. Electrochem. Soc.* **2016**, *163*, A1373–A1387.
- [35] I. V. Thorat, D. E. Stephenson, N. A. Zacharias, K. Zaghib, J. N. Harb, D. R. Wheeler, *J. Power Sources* **2009**, *188*, 592–600.
- [36] G. F. Dewald, S. Ohno, J. G. C. Hering, J. Janek, W. G. Zeier, *Batteries & Supercaps* **2021**, *4*, 183–194.
- [37] Y. Kato, S. Shiotani, K. Morita, K. Suzuki, M. Hirayama, R. Kanno, *J. Phys. Chem. Lett.* **2018**, *9*, 607–613.
- [38] S. Ohno, C. Rosenbach, G. F. Dewald, J. Janek, W. G. Zeier, *Adv. Funct. Mater.* **2021**, *31*, 1–14.
- [39] K. M. Abraham, *Electrochem. Energy Rev.* **1993**, *38*, 1233–1248.
- [40] K. K. Patel, J. M. Paulsen, J. Desilvestro, *J. Power Sources* **2003**, *122*, 144–152.
- [41] R. B. MacMullin, G. A. Muccini, *AIChE J.* **1956**, *2*, 393–403.
- [42] P. Adeli, J. D. Bazak, K. H. Park, I. Kochetkov, A. Huq, G. R. Goward, L. F. Nazar, *Angew. Chem.* **2019**, *131*, 8773–8778.
- [43] A. Bielefeld, D. A. Weber, J. Janek, *J. Phys. Chem. C* **2019**, *123*, 1626–1634.
- [44] A. Bielefeld, D. A. Weber, J. Janek, *ACS Appl. Mater. Interfaces* **2020**, *12*, 12821–12833.
- [45] S. Ohno, W. G. Zeier, *Acc. Mater. Res.* **2021**, *2*, 869–880.
- [46] D. A. G. Bruggeman, *Ann. Phys.* **1935**.
- [47] B. Tjaden, D. J. L. Brett, P. R. Shearing, *Int. Mater. Rev.* **2018**, *63*, 47–67.
- [48] L. Froboese, J. F. van der Sichel, T. Loellhoeffel, L. Helmers, A. Kwade, *J. Electrochem. Soc.* **2019**, *166*, A318–A328.
- [49] D. Hlushkou, A. E. Reising, N. Kaiser, S. Spannenberger, S. Schlabach, Y. Kato, B. Roling, U. Tallarek, *J. Power Sources* **2018**, *396*, 363–370.
- [50] D. Djian, F. Alloin, S. Martinet, H. Lignier, J. Y. Sanchez, *J. Power Sources* **2007**, *172*, 416–421.
- [51] D. E. Stephenson, E. M. Hartman, J. N. Harb, D. R. Wheeler, *J. Electrochem. Soc.* **2007**, *154*, A1146.

Manuscript received: May 16, 2023

Revised manuscript received: June 16, 2023

Accepted manuscript online: June 19, 2023

Version of record online: July 11, 2023